11-2020

Challenges of Measuring Abyssal Temperature and Salinity at the Kuroshio Extension Observatory

Nathan D. Anderson

Kathleen A. Donohue

Makio C. Honda

Meghan F. Cronin

Dongxiao Zhang

Challenges of Measuring Abyssal Temperature and Salinity at the Kuroshio Extension Observatory

NATHAN D. ANDERSON,[a,b] KATHLEEN A. DONOHUE,[c] MAKIO C. HONDA,[d]
MEGHAN F. CRONIN,[b] AND DONGXIAO ZHANG[a,b]

[a] *Cooperative Institute for Climate, Ocean, and Ecosystem Studies, University of Washington, Seattle, Washington;* [b] *NOAA/Pacific Marine Environment Laboratory, Seattle, Washington;* [c] *Graduate School of Oceanography, University of Rhode Island, Narragansett, Rhode Island;* [d] *Japan Agency for Marine-Earth Science and Technology, Yokosuka, Kanagawa, Japan*

(Manuscript received 9 September 2019, in final form 5 February 2020)

ABSTRACT: The deep ocean is severely undersampled. Whereas shipboard measurements provide irregular spatial and temporal records, moored records establish deep ocean high-resolution time series, but only at limited locations. Here, highlights and challenges of measuring abyssal temperature and salinity on the Kuroshio Extension Observatory (KEO) mooring (32.3°N, 144.6°E) from 2013 to 2019 are described. Using alternating SeaBird 37-SMP instruments on annual deployments, an apparent fresh drift of 0.03–0.06 psu was observed, with each newly deployed sensor returning to historical norms near 34.685 psu. Recurrent salinity discontinuities were pronounced between the termination of each deployment and the initiation of the next, yet consistent pre- and postdeployment calibrations suggested the freshening was "real." Because abyssal salinities do not vary by 0.03–0.06 psu between deployment locations, the contradictory salinities during mooring overlap pointed toward a sensor issue that self-corrects prior to postcalibration. A persistent nepheloid layer, unique to KEO and characterized by murky, sediment-filled water, is likely responsible for sediment accretion in the conductivity cell. As sediment (or biofouling) increasingly clogs the instrument, salinity drifts toward a fresh bias. During ascent, the cell is flushed, clearing the clogged instrument. In contrast to salinity, deep ocean temperatures appear to increase from 2013 to 2017 by 0.0059°C, whereas a comparison with historical deep temperature measurements does not support a secular temperature increase in the region. It is suggested that decadal or interannual variability associated with the Kuroshio Extension may have an imprint on deep temperatures. Recommendations are discussed for future abyssal temperature and salinity measurements.

KEYWORDS: North Pacific Ocean; Bottom currents/bottom water; Eddies; Salinity; Temperature; Decadal variability

1. Introduction

Even as scientific curiosity about the oceans and observing technology expands, the deep ocean remains undersampled compared to the upper ocean. As such, the importance of quantifying the abyssal ocean grows in the context of a changing climate. Proceedings of the OceanObs'09 conference addressed this critical need, calling for additional deep ocean measurements and the establishment of high-quality long time series (Fischer et al. 2010), ultimately leading to the formation of the Deep Ocean Observing Strategy (DOOS; http://deepoceanobserving.org). Responding to this call for deep ocean observations, the OceanSITES program (http://www.oceansites.org) proposed expanding the capabilities of existing mooring sites by incentivizing deep temperature and salinity (*T*/*S*) sensor deployments. As part of the OceanSITES "deep *T*/*S* challenge," each group contributing an instrument receives a matching instrument contributed to the OceanSITES pool by industry and agency donors (Levin et al. 2019). As of June 2019, the OceanSITES web page reports near-full utilization of the matching pool instruments. A total of 58 previously existing deep sensors, with 24 newer installations and 6 planned deployments, has brought the deep *T*/*S* challenge close to its goal of 100 moored sensors below 2000 m worldwide.

The Kuroshio Extension Observatory (KEO) moored surface buoy has included measurements of bottom temperature and salinity since mid-2013. Initiated in 2004 as a long-term OceanSITES reference station in the northwestern Pacific Ocean, KEO is sited within the southern recirculation gyre of the Kuroshio Extension (KE) current (Fig. 1). Decadal variations in the state of the KE system have been associated with the dynamic phase (stable versus unstable) of the KE (Qiu et al. 2014), the Pacific decadal oscillation (Qiu and Chen 2010; Qiu et al. 2015), and eddy kinetic energy (Yang et al. 2017), with large *T*/*S* anomalies subducted in the main thermocline of the upper 1000 m during the stable phase (Qiu and Chen 2006; Rainville et al. 2014). Much less is known, however, about the precise deep *T*/*S* response to variations in the KE state.

This paper seeks to differentiate real and false signals in deep sensor records at KEO. Western boundary currents (WBCs) such as the Kuroshio Extension potentially provide a pathway for deep ocean water mass anomalies, but are also prone to benthic storms, which can loft sediment with deleterious

---

Denotes content that is immediately available upon publication as open access.

Supplemental information related to this paper is available at the Journals Online website: https://doi.org/10.1175/JTECH-D-19-0153.s1.

Corresponding author: Nathan D Anderson, nathan.anderson@noaa.gov

DOI: 10.1175/JTECH-D-19-0153.1

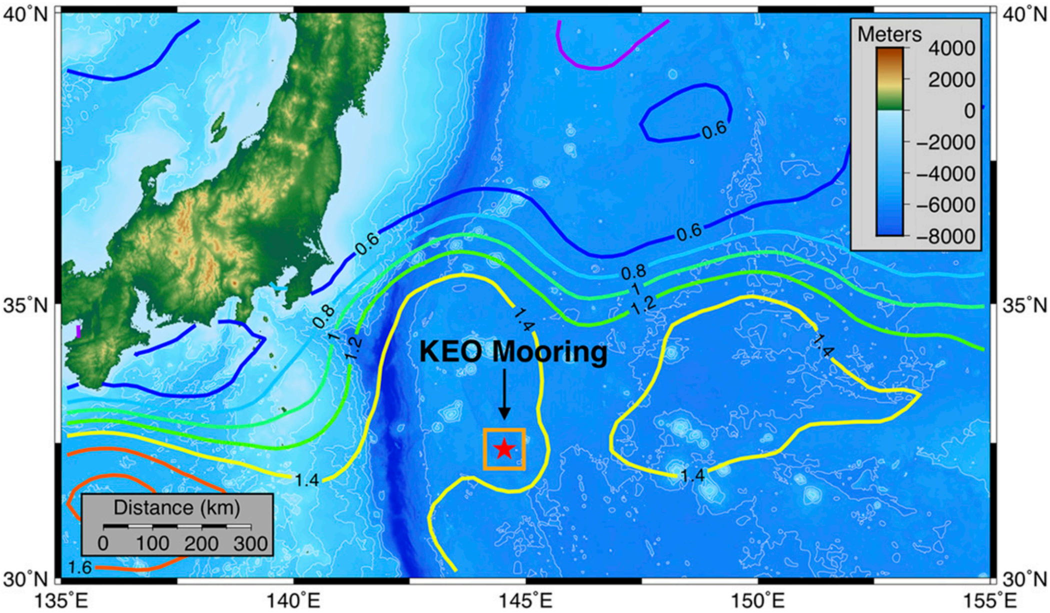

FIG. 1. KEO regional map, with Smith and Sandwell (1997) bathymetry (color shades). Sea surface height (SSH) is contoured every 0.2 m. SSH is from the AVISO Data Unification and Altimeter Combination System (DUACS) 2014 global, delayed-time, gridded, two-satellites-merged product and can be interpreted as surface geostrophic streamlines of flow. The Kuroshio Extension can be identified by the tightly packed SSH contours extending east from Japan.

effects on data quality. Benthic storms were observed in the Kuroshio Extension System Study (KESS) and are discussed in the context of jet instability (Waterman et al. 2011), relationship to external variability and KE meanders (Greene et al. 2012; Tracey et al. 2012), and upper water column eddy heat fluxes (Bishop et al. 2013). Baroclinic instability within the Kuroshio jet could generate full water-column benthic storms, as shown in WBC modeling studies (Schubert et al. 2018; Cronin et al. 2013; Kämpf 2005), and wind stress may further contribute to benthic storm formation (Quirchmayr 2015). Other studies have explored the physical and biological ramifications of deep-sea storms (Aller 1997; Gage 1996; Gross and Williams 1991), but their impact on instrumentation (e.g., biofouling or sedimentation) is lesser known. Previous research in the Argo community has linked salinity drift to surface fouling (Oka and Ando 2004) and to the length of time spent at the surface (Oka 2005). The deep salinity drifts reported herein are thought to be distinct from conductivity drift caused by upper-ocean biofouling (Ando et al. 2005; Venkatesan et al. 2019), salinity bias due to pressure hysteresis (Ueki and Nagahama 2005), and salinity drift seen in multiyear Argo floats (Thadathil et al. 2012).

Deep temperature and salinity are relatively homogeneous in the North Pacific, in comparison with other basins where deep water is formed. The abyssal North Pacific (below 4000 m) is primarily fed by Antarctic Bottom Water (AABW), and is warming at a rate of 0.002° ± 0.001°C per year, with more significant deep warming in the southern oceans (Purkey and Johnson 2010; Rhein et al. 2013). Warming effects in the North Pacific are conceivably dampened by the large distance from its source region, resulting in a weaker or delayed response to long-term climate signals. While temperature increases are anticipated, changes in deep ocean salinity are less clear regarding sign and magnitude (Heuzé et al. 2015). Accurate ship-based observations are currently available but are sparse in time and space. High-quality, long-term moored time series could therefore fill a critical role in capturing decadal variability.

Here we present 4 years (2013–17) of abyssal *T*/*S* data from the KEO mooring (available at https://www.pmel.noaa.gov/ocs/data/disdel/), plus preliminary data from 2018 to 2019, to provide lessons learned that may help to improve deep ocean data quality. This paper is organized as follows. Section 2 describes the regional setting using observations from KESS and JAMSTEC. Section 3 introduces the SBE37 instrumentation used at KEO and details about the KEO abyssal *T*/*S* time series. Section 4a analyzes a 0.0059°C warming trend over the 2013–17 record, which represents interannual variability possibly related to changes in the state of the Kuroshio Extension system. Section 4b describes an apparent freshening drift ranging from 0.03 to 0.06 psu observed during each deep *T*/*S* deployment and argues that this fresh drift is likely caused by sediment buildup that is due to the deployment of sensors within the nepheloid layer. Section 5 concludes with recommendations for best practices for long-term, moored *T*/*S* measurements and discusses implications for DOOS.

2. Regional setting

The KESS experiment (June 2004–June 2006; detailed in Donohue et al. 2008) provides regional context for deep ocean

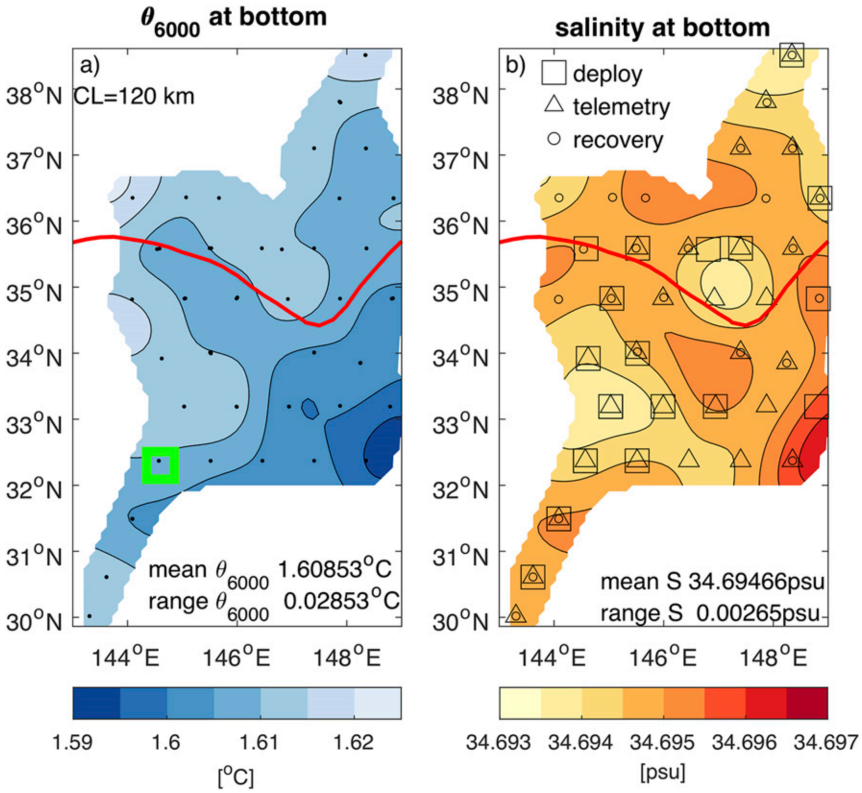

FIG. 2. Mapped (a) θ_{6000} and (b) salinity bottom samples from the KESS CTDs (black dots) during deployment, telemetry, and recovery cruises (2004–06). The red line represents the Kuroshio Extension axis during KESS observations, as in Bishop et al. (2013). The green square denotes the location of the KEO mooring.

properties. The study aimed to understand the dynamics of the Kuroshio Extension and associated recirculation gyres. Observations included 46 current- and pressure-recording inverted echo sounders (CPIES) and eight subsurface moorings deployed for 2 years to the east of Japan, in the region of highest surface eddy kinetic energy. CPIES temperatures are precise but have poor accuracy, so while CPIES temperature variations could be assessed with respect to KEO abyssal temperatures, no absolute temperature intercomparisons were possible. Tracey et al. (2017) provide further details about the CPIES bottom temperature measurements.

Additional near-bottom KESS measurements included full water column hydrocasts taken on deployment, telemetry, and recovery cruises at a subset of CPIES locations. Deep temperature and salinity from hydrocasts are shown in Fig. 2. Temperatures are presented as potential temperature adjusted to 6000 dbar (hereinafter θ_{6000}). Temperature and salinity within 20 m of the seafloor were extracted from KESS cruise hydrocasts in June/July 2004, July 2005, and July 2006 to calculate θ_{6000}. The deep temperature and salinity maps in Fig. 2 were made using optimal interpolation (Bretherton et al. 1976) with a Gaussian correlation length scale of 120 km and should be interpreted as a 2-yr smoothed climatology. The red line in Fig. 2 represents the Kuroshio Extension axis during KESS observations in the 144°–148°E region, determined by Bishop et al. (2013), and corresponds to the sea surface height contour coincident with the maximum sea surface height gradient contour, as in Bishop et al. (2013). Deep salinity (and potential temperature) in Fig. 2 spans 0.003 psu (0.028 53°C), with the coldest and most saline waters found in the deepest, southeastern portion of the array. Figure 3a shows standard deviations of 3-day low-pass (fourth-order Butterworth) filtered CPIES near-bottom temperatures, smoothed with a correlation length scale of 120 km. The range of standard deviations in Fig. 3a is 0.006°C, with slightly elevated values near the center of the array. Near bottom eddy-kinetic energy (EKE), adapted from Fig. 4c in Park et al. (2008), is highest in the central part of the array beneath the mean KE standing trough (Fig. 3b), where benthic storms are active. The relationship between temperature variability and EKE is tenuous. Unlike bottom pressure and currents, the CPIES bottom temperatures are poorly correlated with each other site to site, indicating that deep temperature is better interpreted as a tracer rather than a dynamical variable. Deep temperature and salinity contour plots show that the horizontal gradients in temperature and salinity are particularly weak near the region of elevated near-bottom EKE (Figs. 2 and 3). Enhanced horizontal stirring associated with benthic storms is a possible explanation for the weak gradients.

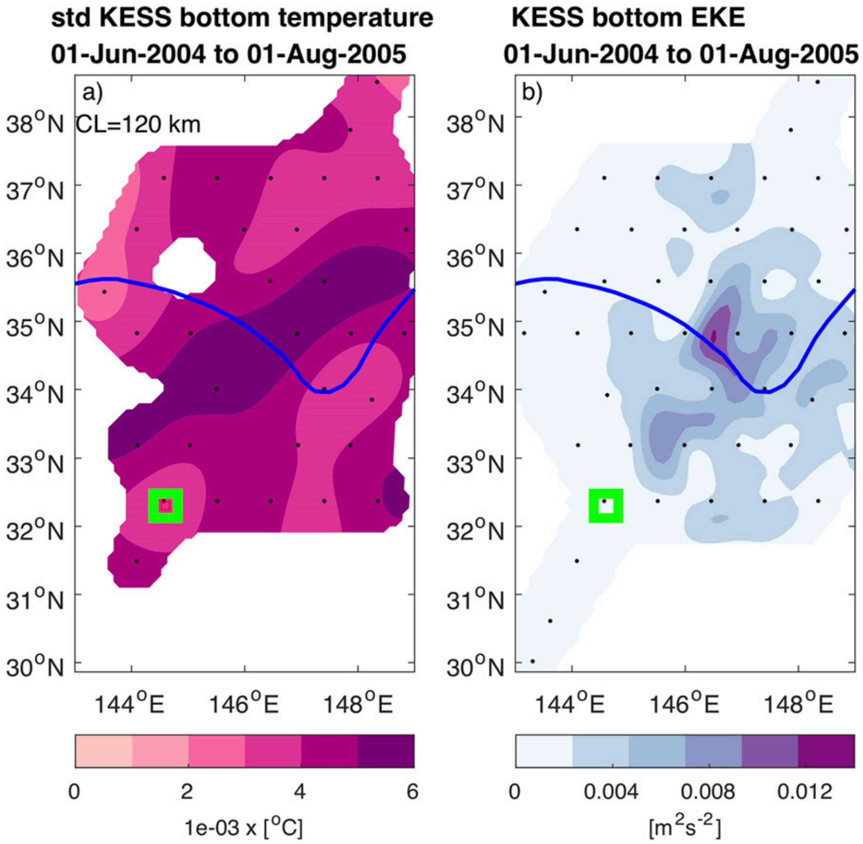

FIG. 3. (a) Standard deviation of 3-day low-pass-filtered CPIES bottom temperature measurements with continuous record lengths longer than 18 months (black dots). (b) Deep eddy kinetic energy from the KESS moored array, adapted from Park et al. (2008, their Fig. 4c). The blue line represents the Kuroshio Extension axis during KESS observations as in Bishop et al. (2013). The green square denotes the location of the KEO mooring.

In addition to five JAMSTEC casts (JAMSTEC database DARWIN; http://www.godac.jamstec.go.jp/darwin/datatree/e) contemporary with the deep KEO *T*/*S* time series presented here, the NSF-funded KESS study provided three WOCE-quality (WCRP 1988) CTD hydrocasts near KEO, two in 2004 and one in 2005 (KESS data products; https://cchdo.ucsd.edu/search?q=KESS). Full-depth hydrocast locations in the KEO region are displayed in Fig. 4. The CTD casts show that vertical gradients of temperature and salinity are weak in the deep ocean, and the increasing homogeneity with depth manifests as asymptotic profiles in Fig. 5. Potential temperature decreases with depth, at a rate that approaches zero near the seafloor, coinciding with temperature increases of 0.000 10°–0.000 14°C dbar^{-1} in each cast's lowest 100 dbar. Vertical salinity gradients also become exceedingly small in the deep ocean. Salinity changes in the lowest 1000 dbar of the casts ranged from 0.0029 to 0.0038 psu, corresponding to an average salinity increase of from 2.9×10^{-6} to 3.8×10^{-6} psu/dbar during descent. Thus, compared to the temperature trend and salinity drift anomaly presented herein, variations in mooring depths (see pressure in Fig. 6d) are insignificant in the context of vanishingly small vertical gradients.

JAMSTEC has also maintained a sediment trap adjacent to the KEO mooring (Fig. 4), at a depth of 4900–5000 m, or about 800 m above the ocean floor in 5700–5800 m of water (details in Honda et al. 2018).

3. Deep SBE37 instruments at KEO

Since 2013, the KEO measurement suite has included a SeaBird Scientific SBE37-SMP, with sensors measuring temperature, conductivity, and pressure (*T*/*C*/*P*) attached to the acoustic release on the KEO mooring line at approximately 56 m above the ocean floor (hereinafter aof). Two instruments (one per deployment, except for a failure in 2017 and one failure in 2018, when three instruments were deployed) are rotated annually during KEO mooring maintenance operations. Deployments precede recovery to provide overlapping records that ensure time series continuity and a data verification window, requiring each mooring to occupy a new location. KEO is a slack line mooring, but a series of 18 flotation spheres at approximately 90–100 m aof keep the deep instrument at a relatively stable depth, with occasional depth excursions when strong currents or tensions tilt the mooring line. Pressure is measured by a Kistler piezoelectric pressure sensor on the

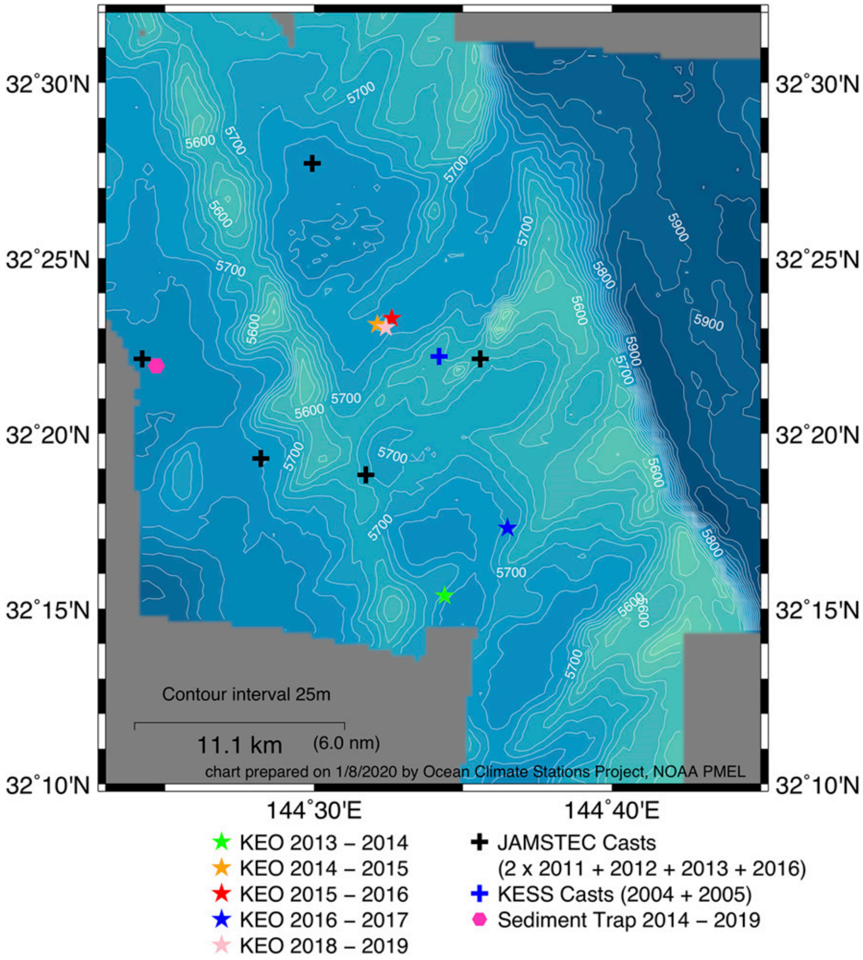

FIG. 4. KEO mooring locations (color-coded stars) over the study period, excluding the failure in 2017. Bathymetry is from the Japanese R/V *Mirai*, contoured every 25 m in depth and labeled every 100 m. Full water-column hydrocasts from KESS (blue) and JAMSTEC (black) are denoted by crosses. The JAMSTEC sediment trap is shown as a magenta hexagon.

SBE37, and although deployment depths can vary between deployments due to terrain or line length variations, pressures align with bathymetry, with no discernible, yearlong pressure drift observed (no slope in Fig. 6d). Temperature is measured with a thermistor, and conductivity is measured by assessing the resistance between 3 internal platinum electrodes within a conductivity cell made of borosilicate glass encapsulated by a urethane covering. Unpumped SBE37s were used in this study, although a pumped version is currently being tested, which actively moves water through an inverted U-shaped (rather than the unpumped version's vertically oriented) conductivity cell. The SBE37s feature an antibiofoulant plug near the conductivity cell to reduce biofouling. Figure 7 shows the version of the SBE37s used in the 2018 deployment, with both the standard unpumped instrument and the additional pumped instrument. Measured conductivity, temperature, and pressure are combined using the UNESCO equations (Fofonoff and Millard 1983) to compute θ_{6000} and practical salinity, the latter of which is output by the instrument itself but can be calculated in postprocessing if combining calibrations (see the next paragraph).

SeaBird performs annual temperature, pressure, and conductivity calibrations before deployment (precalibration) and after recovery (postcalibration). The postcalibration serves as the precalibration for the next deployment if no alterations are made, and calibration records indicate that no conductivity cell electrode replatinization was required during this study. The uniformity of the beginning values in each salinity record attests to the consistency of calibrations. In standard data processing, time series are interpolated to reflect the application of conductivity precalibration coefficients at the start, and postrecovery calibration coefficients at the end of the deployment. However, with minimal differences between the "postcal" and "precal" data, only the precal data directly from each instrument were used, with the postcal considered a check. The maximum salinity offset between calibrations was 0.0053 psu,

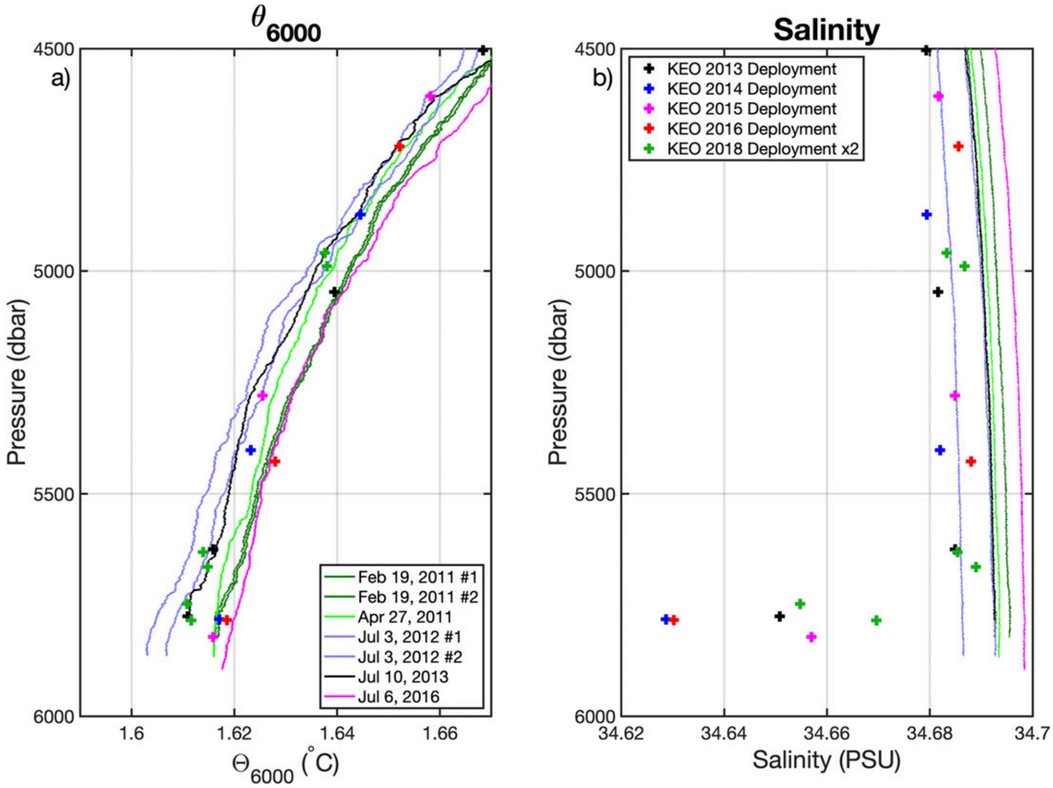

FIG. 5. Regional JAMSTEC hydrocasts from 2011 to 2016 remain remarkably consistent, despite inherently capturing KEO's spatial and temporal variability at depth. For KEO, (a) θ_{6000} and (b) the year's cumulative salinity drift are highlighted by plotting one data point before the acoustic release is triggered, along with measurements made during ascent from the SBE37 recoveries.

and the maximum temperature offset between calibrations was 0.002°C, indicative of postcalibration consistency with each instrument's predeployment state.

Deployment positions are plotted in Fig. 4 and time series are shown in Fig. 6. KEO positions vary slightly (<15 km) about a nominal location of 32.3°N, 144.6°E, and a nominal depth range of 5640–5720 m. Sensors were programmed to make instantaneous 10-min spot samples, and general instrument specifications are provided in Table 1. SeaBird only provides accuracy specifications for conductivity, temperature, and pressure, but a salinity overview can be found in Freitag et al. (1999), which specifies a conservative salinity accuracy of 0.02 psu.

Overlapping data from deployments were spliced into a continuous time series. Transition times were selected to optimize data handoff, balancing new sensor equilibration times with old deployment terminations. New deployment equilibration times were maximized by waiting to utilize the new deployment until within 30 min of the old deployment's final measurement at depth (exact times are presented in Table 2). The θ_{6000} from the last 10-min time stamp before a deployment transition was compared to θ_{6000} at the corresponding time stamp of the new deployment. The maximum absolute difference was less than 0.0001°C, an order of magnitude below instrument accuracy specifications, lending confidence that the accuracy of temperature and pressure measurements exceeds manufacturer specifications. RMS differences of θ_{6000}, comparing data from the final hour of one deployment with the same time stamps from the next deployment, were similarly small (Table 2).

4. Results and discussion

a. KEO bottom temperature trend

KEO near-bottom potential temperatures increase slightly over the 4-yr contiguous record from 2013 to 2017 (Fig. 8). A linear regression produces a slope of 0.0015°C per year, or 0.0059°C over the period. While this trend is statistically significant (the null hypothesis is rejected at the 99% confidence level, with a p value <0.01) and in alignment with basinwide warming rates (Purkey and Johnson 2010), KESS CTD abyssal temperatures and SBE37 temperatures from 2018 to 2019 show that the trend does not extend back or forward in time (Fig. 9a).

Mean θ_{6000} from the three KEO-proximity KESS CTDs is 0.0120°C warmer than predicted from the linear fit to the KEO data (0.0146°, 0.0104°, and 0.0109°C warmer for April 2004, May 2004, and June 2005 casts, respectively, corresponding to 4.1, 2.9, and 3.1 times the standard deviation of the detrended θ_{6000} time series), further suggesting that extrapolation of the linear regression back to the time frame of KESS is unrepresentative of temperatures at that time. Note that these

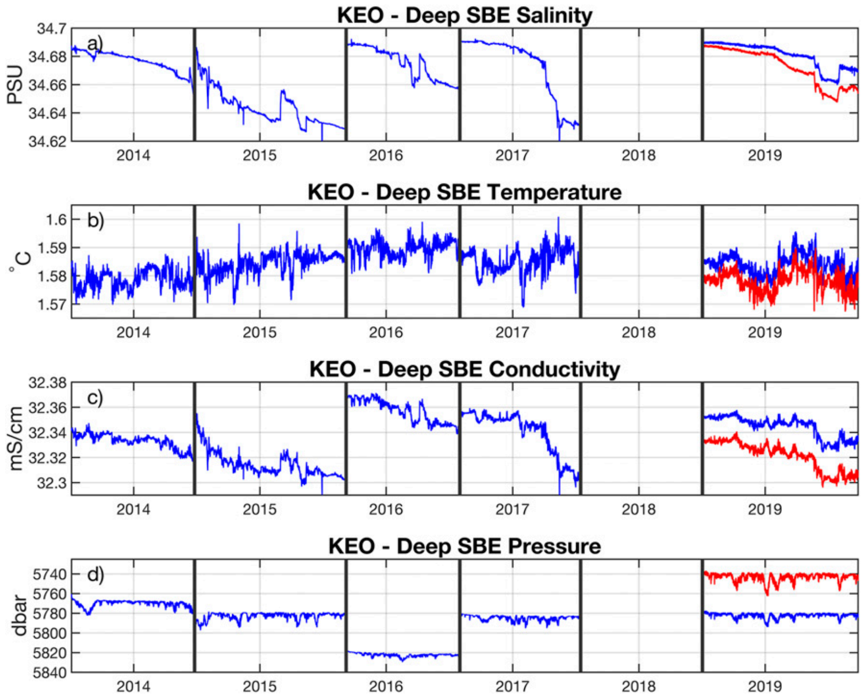

FIG. 6. In situ time series of (a) salinity, (b) temperature, (c) conductivity, and (d) pressure from the SBE37s at 56 m aof (blue). Vertical lines denote mooring deployments, with data during ascent/descent removed. A 2017 failure resulted in no data, and an additional SBE37 was deployed at 90 m aof (red) in 2018 (a third, also at 56 m, experienced a salinity sensor failure and is not shown).

cast values are from ~10–20 m aof and are not exactly coincident with KEO's SBE37 depths. Nevertheless, the difference between KESS and KEO is not due to small differences in sensor depth. A 0.0120°C difference would require a depth difference of about 100 dbar, given typical temperature lapse rates (and >100 dbar, given deep θ_{6000} lapse rates). Figure 9a shows these casts (black asterisks) in context with the deep SBE37.

Pressure-adjusted temperatures (θ_{6000}) were also obtained or computed from the JAMSTEC deep CTDs (JAMSTEC database DARWIN; http://www.godac.jamstec.go.jp/darwin/datatree/e). These casts averaged 0.0043°C warmer than the KEO linear fit (0.0094°, 0.0102°, −0.0040°, 0.0009°, and 0.0052°C warmer for February 2011, April 2011, July 2012, July 2013, and July 2016, respectively). Data were taken from each cast at 5780 dbar to approximate the moored SBE37's depth. Again, Fig. 9a shows these casts (magenta asterisks) in context with the deep SBE37.

A reasonable hypothesis is that the apparent 2013–17 temperature trend reflects interannual or decadal variability in the KE system. Previous work characterized the state of the Kuroshio Extension with an index called the "KE index" (Qiu et al. 2014), which may be found at http://www.soest.hawaii.edu/oceanography/bo/KE_index.asc. A high KE index indicates a strong southern recirculation gyre and KE jet, a northerly KE position, and low KE jet meandering. The KE index was high and slowly decreasing from 2013 to 2017, a period of generally increasing temperatures (Figs. 8–10). After averaging θ_{6000} temperatures to match the weekly time stamps of the KE index (from 3.5 days before to 3.5 days after, to center about each KE index time stamp), a three-point moving average was passed over both time series to reduce small-scale noise. An inverse correlation (−0.53) was found between the smoothed KE index and θ_{6000} (Fig. 10). The null hypothesis ($\rho = 0$, which hypothesizes a zero slope) was tested, and degrees of freedom were calculated using the method of Bretherton et al. [1999, their Eq. (31)]. The absolute t value of 9.1 exceeded the critical t value of 2.2, and the null hypothesis was rejected (indicating a nonzero slope) at a statistically significant 95% confidence level using a two-tailed Student's t test. A possible conclusion is that surface properties captured in the KE index are reflected in deep ocean temperature.

We speculate that increased abyssal temperatures could be attributed to changes in the KE jet represented by the KE index. A low KE index, with increased jet meanders and more energetic eddies, is likely to produce higher deep velocities. Bottom velocities observed during KESS showed seafloor currents frequently near 10 cm s^{-1}, with occasional velocities over 30 cm s^{-1}. Combined with the regional temperature range of 0.03°C in Fig. 2, advection could explain the weekly-to-monthly-scale bottom temperature variability seen in Figs. 6 and 8–10. Increased vertical diffusivity caused by elevated deep velocities interacting with topography is another possible mechanism for the warming. The KE system did not undergo a

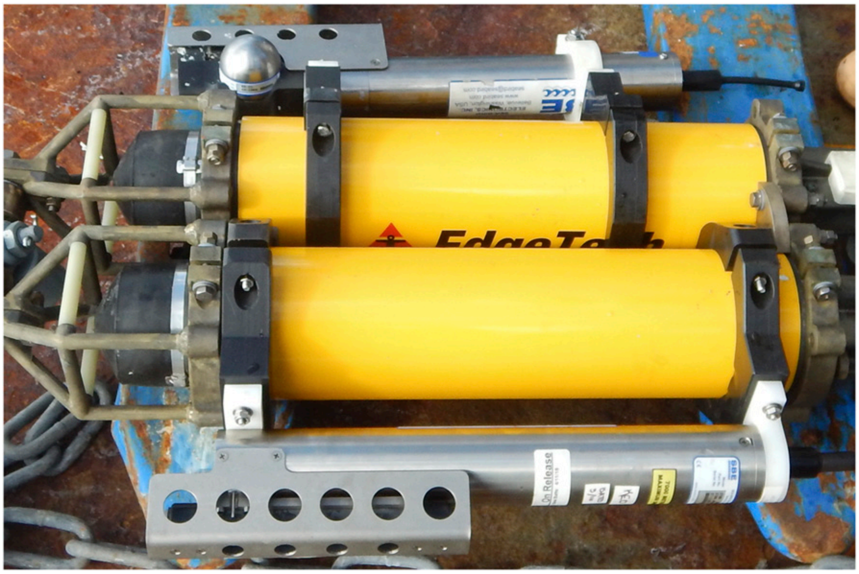

FIG. 7. Two SBE37s attached to the dual acoustic releases. Pictured is the 2018 deployment, with the standard unpumped instrument at the bottom of the photograph and the additional pumped instrument at the top that sits at 56 m aof. The shield and body total 17.6 in. (44.7 cm), excluding the end plug.

large transition in state during the 2013–17 time frame, so additional years of KEO deep temperature measurements may be required to more definitively link the KE index to deep temperature trends.

The nearby S1 site, a former JAMSTEC time series station located south–southeast of KEO at 30.1°N, 145.0°E, does not show an increasing temperature trend (Fig. 11), supporting the idea that KEO's observed 2013–17 temperature trend is driven by the Kuroshio Extension, despite alignment with basinwide warming rates (Purkey and Johnson 2010). Studies suggest the southern Pacific warming trend is accelerating (Johnson et al. 2019; Purkey et al. 2019) and that planetary waves can quickly transport temperature anomalies to the North Pacific (Masuda et al. 2010).

Temperature spectra revealed cyclic patterns in the KEO θ_{6000} data (Fig. 12). The KEO θ_{6000} record was first low-pass filtered with a 3-day, fourth-order Butterworth filter to reduce high-frequency signals, then subsampled to every 12 h. Variance-preserving spectra were computed using Welch's method with a Hanning-windowed 366-day FFT length and 50% overlap. The 95% confidence intervals in Fig. 12 were calculated using an inverse chi-squared probability density function. The noncontinuous 2018–19 data were not included in the spectral analysis. Spectral peaks in the mesoscale-frequency band near 1/37 and 1/23 cycles per day (cpd) offer the intriguing possibility that regularly occurring benthic storms have an imprint on bottom temperature. Further, Na et al. (2016) demonstrate that barotropic ocean variability in the KESS region within the mesoscale band (1/60–1/7 cpd) is driven by both oceanic and atmospheric (primarily wind stress curl forcing) processes. Investigation of the nuanced relationship between surface meteorological influence, mesoscale ocean variability, benthic storms, and deep temperature may become a new focus as deep ocean climatology develops.

b. KEO bottom salinity drift

While each deployment exhibits a freshening trend, there is a striking discontinuity between the end of the deployment record and the beginning of the newly deployed record, suggesting that the freshening trend is due to a sensor problem (Fig. 6a). The freshening drift of from −0.03 to −0.06 psu per year occurs with each sensor deployment. Each alternated SBE37 instrument exhibits this salinity drift, so factors common to each sensor contribute to the apparent drift. The stark discontinuity is present regardless of whether precalibration or postcalibration coefficients are applied.

TABLE 1. Manufacturer specifications for the SeaBird Scientific SBE37 instrument. SeaBird does not supply a salinity accuracy, but experience-based performance and a PMEL technical memorandum suggest accuracy to 0.02 psu (Freitag et al. 1999).

	Measurement range	Initial accuracy	Stability	Resolution
Conductivity	0–7 S m^{-1}	± 0.0003 S m^{-1}	0.0003 S m^{-1} month^{-1}	0.000 01 S m^{-1}
Temperature	From −5° to 45°C	± 0.002°C	0.0002°C month^{-1}	0.0001°C
Pressure	7000 m	± 0.1% range	0.05% range yr^{-1}	0.002% range

TABLE 2. Overlapping data from deployments were spliced into a single time series using the following start/end times. RMS differences between overlapping measurements were calculated for the 1 h of 10-min records closest to a deployment's end (and not release time). With no 2017–18 data for context, preliminary 2018–19 (serial numbers 11926 and 12243) data began 2 h after anchor drop and ended with the final data point at depth before ascent.

	KE011	KE012	KE013	KE014
Start	0540 UTC 5 Jul 2013	2340 UTC 25 Jun 2014	0650 UTC 7 Sep 2015	0050 UTC 1 Aug 2016
End	2330 UTC 25 Jun 2014	0640 UTC 7 Sep 2015	0040 UTC 1 Aug 2016	0510 UTC 16 Jul 2017
Serial number	10504	11926	10504	11926
Release time	2339 UTC 25 Jun 2014	0648 UTC 7 Sep 2015	0110 UTC 1 Aug 2016	0527 UTC 16 Jul 2017
RMS diff (θ_{6000}), final 1 h		0.000 168°C	0.000 295°C	0.000 392°C

Curiously, the fresh offset quickly abates during the sensor's approximate 1 m s^{-1} ascent through the water column during recovery. In the first 10-min SBE37 sample during ascent, the offset between regional hydrocasts and the SBE salinity decreases to less than 0.01 psu (Fig. 5b). Each deployment showed this pattern of immediate and near-complete recovery after the acoustic release was triggered, suggesting the conductivity cell gets flushed during ascent.

Two potential culprits responsible for the apparent salinity drift are easily dismissed: pressure sensor drift and compression of the conductivity cell. The conversion from conductivity to salinity, and the conductivity measurement itself, requires accurate pressure measurements. A constant internal SeaBird parameter (CPcor) scales conductivity to account for compression of the conductivity cell, but could not cause salinity drift in the absence of pressure drift. CPcor issues would present as a linear, gradual recovery during ascent, rather than the immediate restoration of accuracy seen in Fig. 5. The rapid recovery while still under pressure in the first data point during ascent, combined with the absence of a similar salinity effect at nearby station S1 (>6000 m), likely discounts any gradual, geometrically distorting effect of pressure on the conductivity cell. Using the UNESCO equations (Fofonoff and Millard 1983), about 80 dbar of pressure drift would be required to alter salinity by the minimum 0.03-psu drift. This is an unrealistic pressure drift, given the physical constraints of the mooring. Although KEO is a slack line mooring, the SBE37 is bound to the anchor by 56 m of line and hardware that is kept taut by flotation spheres.

Two hypotheses are put forward that could independently or jointly explain the fresh drift, rapid recovery, and consistent calibrations: 1) *sediment accumulation* in the sensor and 2) *biofouling* from a bacterial film. Both hypotheses reduce the cross-sectional area of the conductivity cell, artificially reducing conductivity and causing the apparent conductivity/salinity drift. Although less biofouling occurs with depth in the upper ocean, deep biofouling remains a possibility, as a variety of benthic species and their response to benthic storms have been documented (Aller 1997; Gage 1996). SeaBird, Inc., found that a 1.5–3.1-μm constriction of the conductivity cell's radius could lower salinity by 0.03–0.06 psu (K. Martini and D. Murphy 2018, personal communication). The equation for calculating conductivity inside a fouled cell is $C_f = C \times R^2/(R - B)^2$, where C is conductivity, C_f is the conductivity measured by a fouled sensor, R is the conductivity cell's radius (0.004 m), and B is the thickness of the biofouling or sediment. All distances are in meters and conductivities are in millisiemens per centimeter. Conductivity values were calculated for salinities of 34.68, 34.65, and 34.62 psu to simulate the 0.03–0.06-psu drifts (the small discrepancy between casts and deep SBE37s in Fig. 9b is not addressed here). Temperature and pressure were held constant at 1.58°C and 5780 dbar to mimic deployment conditions. The calculated conductivities of 32.340, 32.315, and 32.290 mS cm^{-1} result in the thickness range introduced above (B = 1.5–3.1 μm) to explain the salinity drifts seen at KEO.

Two additional aspects of the KEO SBE37 drift are worth pointing out here. First, the abyssal KEO salinity drift does not appear to have the same magnitude deployment to deployment.

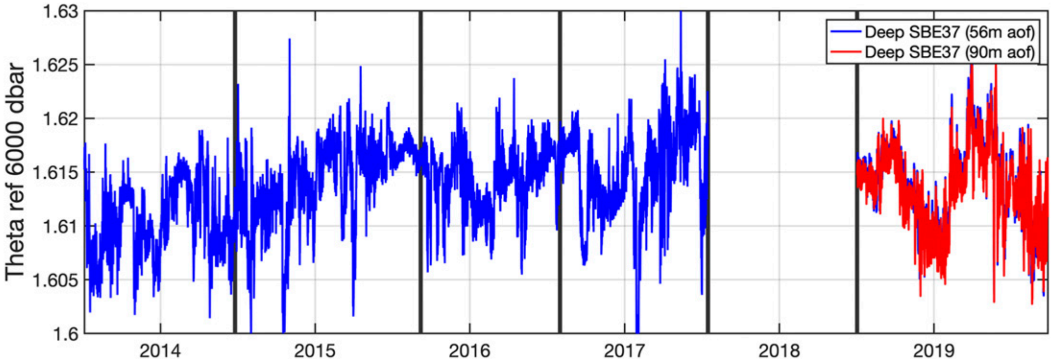

FIG. 8. Potential temperature (θ_{6000}) from the SBE37 deployments. Vertical dark lines indicate the annual mooring service, with one instance of instrument failure in 2017 and subsequent redundancy in 2018. Note the continuity of θ_{6000} as compared with raw temperatures in Fig. 6b.

For example, in the first 8 months of the 2014–15 deployment, salinity decreases by about 0.05 psu while during the first 8 months of the 2016–17 deployment, salinity decreases by only 0.01 psu. Second, during each year, the slow decrease in salinity is punctuated by rapid increases in salinity. For example, in late February 2016, salinity increases by 0.0081 psu in 10 min, and in early April 2016, salinity increases by 0.0180 psu in 10 min. In other words, measurement quality undergoes slow deterioration, followed by occasional but rapid self-corrections. In each case, the magnitude of the self-correction is not large enough to bring the measurement back into reasonable territory. The conductivity cell's vertical orientation could explain why ascent effectively flushes the conductivity cell, while deep horizontal currents (potentially enhanced by tilting) ineffectively flush the cell during partial self-correction events. Self-corrections could also relate to periodic ''cool events,'' marked by cooler temperatures and greater pressures witnessed in the SBE37 data (Figs. 6 and 8). Given the weak vertical gradients at depth and small vertical excursions of the SBE37, these cool events are attributed to deep ocean variability. Pinpointing the exact cause of small-scale variability is outside the scope of this paper, but possibilities include internal waves generated at topography, wind-driven near-inertial waves, or advective events associated with benthic storms. Note that Park et al. (2010) found weak near-inertial signals at depth south of the KE axis, showing that the KE effectively blocks the equatorward propagation of wind-driven inertial waves. Benthic storms or internal waves potentially explain both 1) the high-frequency temperature fluctuations, and 2) the salinity self-corrections, as currents partially flush the cell yet are liable to loft additional bottom sediment. As the disturbance subsides, the still, turbid waters remain, speeding future accumulation (i.e., drift) in the cell. Small-scale features in Fig. 6 confirm that cool events and self-corrections often precede a period of intensified fresh drift. Regardless, the sporadic nature of self-corrections complicates efforts to detrend or correct the data.

Evidence of suspended sediment (i.e., a nepheloid layer) in the water column at KEO comes from the JAMSTEC sediment trap. The sediment trap primarily captures descending sediment originating from the surface, but also captures particles characteristic of laterally transported bottom sediment (Fig. 13), indicative of strong currents suspending particles from the seafloor. When bottom-sourced particles are detected in the sediment trap at 800 m aof, the nepheloid layer must exceed 800 m, also placing the SBE37 (56 m aof) within the nepheloid layer. Combined with no physical evidence of biofouling on the recovered deep sensors and the presence of an antibiofoulant plug, this suggests a preference for the sediment hypothesis.

Nepheloid layers fundamentally have three sources: surface settling, seafloor scouring/suspension, and particle advection (Gardner et al. 2017). Variations in each can lead to diverse particle concentrations, nepheloid layer depths, and chemical compositions. Topography can influence currents to further enhance or diminish the patterns of sediment entrainment or deposition. Sites known to experience high abyssal eddy kinetic energy, variable bathymetry, or strong western boundary currents are candidates for nepheloid layer presence and enhanced particle loads (Gardner et al. 2017; Cronin et al. 2013; Richardson et al. 1993; McCave 1986; Hollister and McCave 1984). Instruments deployed into these conditions have increased potential for salinity drift. Since KEO fits this description, continued monitoring of the KEO region is warranted to identify if particular nepheloid layer properties disproportionately contribute to the SBE37 salinity drift. Deep current meters and nephelometers would be valuable additions to future research. Interestingly, Gardner et al. (2018a,b) reported weaker benthic nepheloid layers in the Kuroshio region and away from continental margins, contrary to the sediment trap data described below.

Benthic storms, which are full water-column cyclones capable of scouring and lofting seafloor sediment, likely generate and maintain thick nepheloid layers. Intense, relatively long-lasting benthic storms are a common feature of western boundary current regions (Cronin et al. 2013; Schubert et al. 2018). A thick nepheloid layer associated with benthic storms at KEO could cause the conductivity cell to accumulate sediment, artificially reducing conductivity and salinity. Persistent salinity drift at KEO also suggests that thick nepheloid layers are long lived in the KEO region. Turbidity currents could secondarily contribute to the nepheloid layer but tend to be

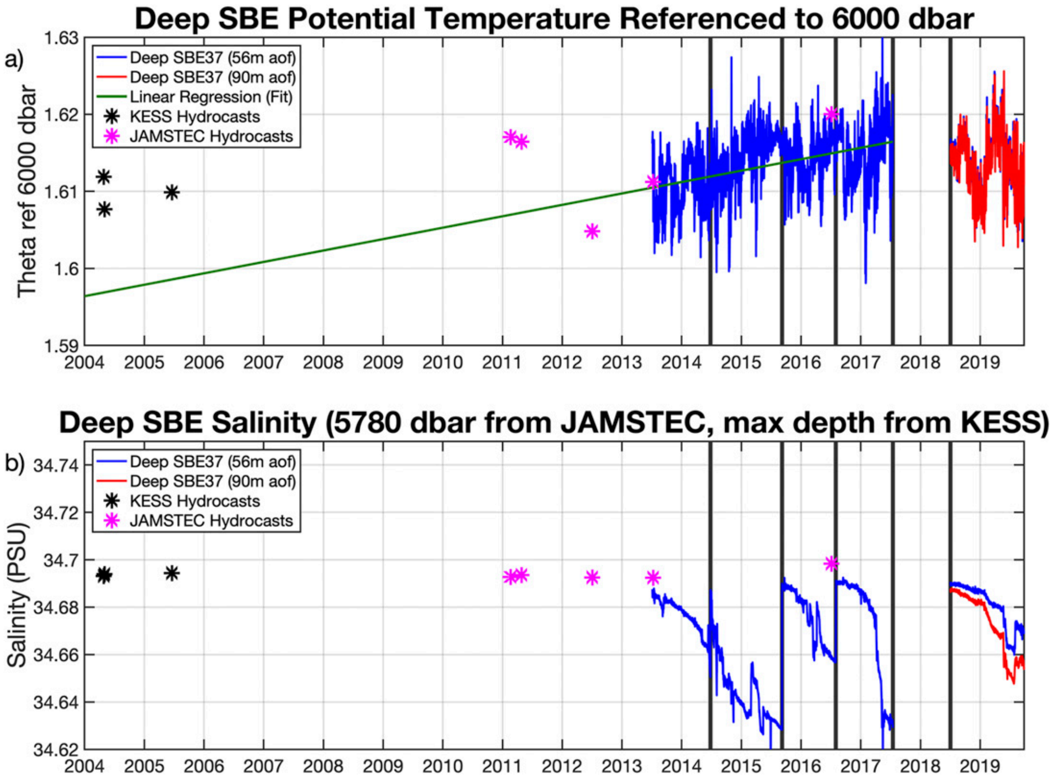

FIG. 9. An extended record of KEO (a) θ_{6000}, as in Fig. 8, but also showing hydrocasts from the previous decade and the mooring θ_{6000} trend of 0.0059°C from 2013 to 2017 extrapolated back in time along its regression line ($y = 0.001\,48 \times \text{year} - 1.371$). The same extended record of KEO with (b) salinity at 56 m aof (blue) and 90 m aof (red) also shows hydrocasts at approximately matching depths from the previous decade, shown with asterisks. Hydrocast bottom depths were 5746, 5732, and 5760 dbar for the KESS hydrocasts (in black) and 5780 dbar for JAMSTEC casts (in magenta). While the moored instruments may have a slight systemic bias vs ship-based casts (also demonstrated in Fig. 11, below), the salinity drift magnitudes overwhelm any SBE-to-hydrocast differences. KESS and JAMSTEC hydrocast locations are shown as blue and black plus signs in Fig. 4. Vertical lines indicate deployment transitions.

more intermittent and isolated to continental shelves. KEO is positioned away from the continental shelf, but some topographic relief near KEO (Fig. 4) could fuel turbidity currents. Regardless, the conclusion stands that near-seafloor sediment is present and is likely responsible for the apparent salinity drift.

Data from the JAMSTEC-owned KEO sediment trap reveal clues about the frequency and intensity of benthic storms. While the total mass flux detected by the sediment trap was typical of surrounding regions, high lithogenic material (alumino-silicate) fluxes could be evidence of deep, sediment-laden currents. The mean total mass flux at KEO was calculated as 48.3 mg $\mathrm{m}^{-2}\,\mathrm{day}^{-1}$, with an average of 3.12% aluminum content (KEO sediment trap database; https://ebcrpa.jamstec.go.jp/egcr/e/oal/oceansites_keo/). Assuming the average concentration of aluminum in lithogenic material is 8% (McLennan 2001; Honda et al. 2002; Otosaka et al. 2004), the average lithogenic material flux and concentration from July 2014 through July 2017 was calculated as a relatively high 18.9 mg $\mathrm{m}^{-2}\,\mathrm{day}^{-1}$ (Fig. 13) and 39.0%, respectively. Lithogenic material caught by the sediment trap is likely pelagic red clay, the predominant seafloor constituent in the KEO region (Dr. K. Ikehara, AIST, 2019, personal communication). This is consistent with SeaBird calibration records, which indicate no conductivity cell replatinizations, a procedure often warranted in the presence of diatoms or abrasive sediment. For examples of fluxes at other pelagic stations, see Honda et al. (2002), Francois et al. (2002), or Lamborg et al. (2008).

The localized effect of seafloor sediment on KEO salinity might be supported by the fact that lithogenic material flux at KEO is 2–3 times that at station S1 [7 ± 2 mg $\mathrm{m}^{-2}\,\mathrm{day}^{-1}$ for 2010–14; see the K2S1 database (https://ebcrpa.jamstec.go.jp/k2s1/en/mst.html)]. The S1 site (30.1°N, 145.0°E) was located south of KEO, and significant salinity drift was not observed (Fig. 11).

5. Conclusions and recommendations

KEO deep *T*/*S* measurements are part of a larger scientific effort to quantify the deep oceans and understand climate impacts on isolated systems. Warming trends are beginning to emerge in the deep ocean (Purkey and Johnson 2010) and in WBC regions, where the deep ocean can be very active with strong currents and benthic storms (Zhang et al. 2018). Historically, trends in the deep ocean have been monitored through the

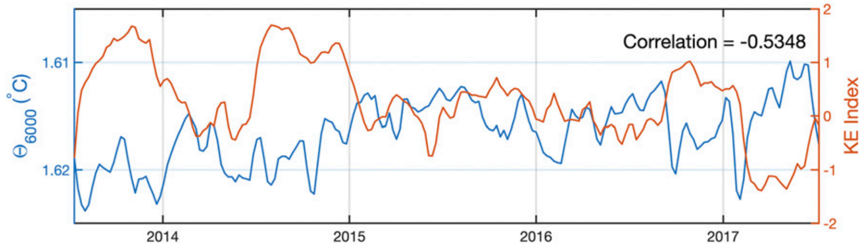

FIG. 10. Weekly mean θ_{6000} and the KE index (at the same resolution) were smoothed with a three-point moving average and showed moderate correlation. The KE index, only available through 2017 as of January 2020, was obtained online (http://www.soest.hawaii.edu/oceanography/bo/KE_index.asc) (Qiu et al. 2014). The null hypothesis (zero correlation) is rejected at the 95% confidence level. A stable or unstable KE system corresponds to a positive or negative KE index, respectively.

Global Ocean Ship-Based Hydrographic Investigations (GOSHIP) repeat hydrographic sections. Going forward, Argo floats are being modified to profile down to the ocean floor (Johnson et al. 2015; Roemmich et al. 2019) and the OceanSITES mooring network has been increasingly instrumented with SeaBird microcat temperature and conductivity (salinity) sensors as part of a deep *T*/*S* challenge. Moorings have the advantage of observing the full spectral range of variability in time, up to the secular trend of the time series.

Deep data from the KEO mooring show a subtle increasing temperature trend. Factors including the interannual/decadal variability in the Kuroshio Extension system could be responsible for the increase in temperature and explain why the 2013–17 trend does not extend back or forward in time. The KE index is a plausible starting point for linking temperature variability to changes in the upper-ocean and the larger KE system. With 4 years of increasing temperatures, and evidence that the trend did not extend back to KESS or forward into

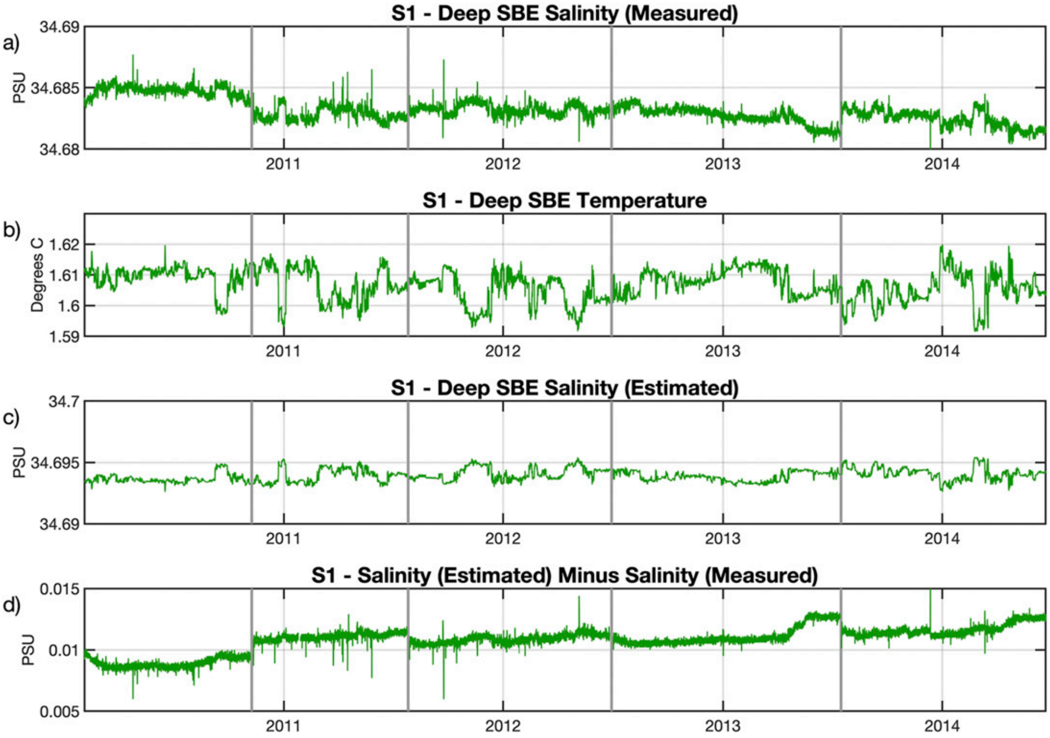

FIG. 11. Plot of deep *T*/*S* time series at S1, operated by JAMSTEC (30.1°N, 145.0°E), with gray lines indicating deployment swaps. (a) Salinity drifts and (b) temperature trends are much more subdued than at KEO, despite a greater depth at S1, likely attributable to the distance from the Kuroshio or to a different phase of the KE index in 2010–14. Since ship-based *T*–*S* relationships cluster more tightly than mooring observations, (c) estimated salinities are computed from the *T*–*S* relationship but are biased toward higher salinity values from hydrocasts (as in Fig. 9b), with (d) differences near 0.01 psu. This figure's data were provided through the courtesy of Dr. H. Uchida (JAMSTEC).

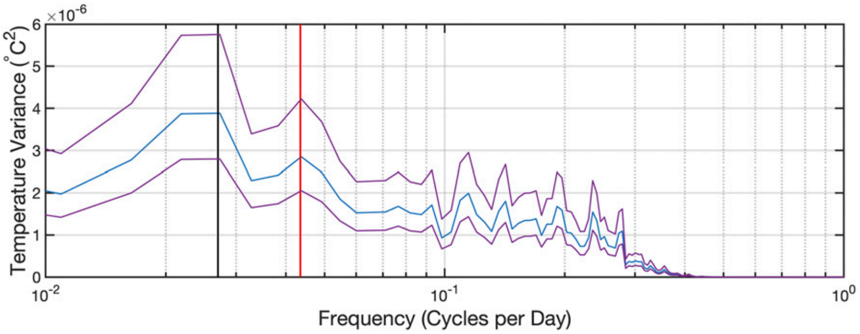

FIG. 12. Variance-preserving spectra using Welch's method, with a Hanning-windowed 366-day FFT length and 50% overlap. KEO θ_{6000} is low-pass filtered with a 3-day, fourth-order Butterworth filter and then subsampled every 12 h before calculating the spectra (blue), with 95% confidence intervals from an inverse chi-square pdf (purple). The red line shows a 23-day peak, and the black line shows a 37-day peak.

the 2018–19 deployment, any cycle would necessarily be part of a longer-term (5–10+ yr) oscillation. An alternative theory is that temperatures were historically more stable, with the 2013–17 data presented here representing the first signal of warmer AABW reaching the North Pacific. Continued deployments are needed to establish long-term site climatology and to separate local WBC effects from subtle changes that arrive via source water advection.

Salinity trends were obscured because of persistent annual conductivity drift during each deployment. We have proposed here that the accretion of bacteria or sediment from a developed nepheloid layer can contaminate conductivity measurements, leading to apparent freshening trends in the moored salinity measurements. The drift is gradual, as mass slowly constricts the conductivity cell of deep instruments at KEO. Observed drift occurs over a yearlong time frame, but is punctuated by partial and brief self-corrections, followed by a more complete correction to within 0.01 psu of average hydrocast profiles in the first 10-min measurement during ascent (Fig. 5). The relatively quick ascent ($\sim$1 m s^{-1}) is thought to wash off accumulated bacteria or sediment. Instrument recovery is further confirmed by the consistency of SeaBird calibrations, and by two comparison casts to 600 m with a calibrated SBE19 immediately after a recovery (not shown).

Several recommendations relevant to the wider DOOS community resulted from the foray into deep ocean measurements at KEO. Future science missions in regions susceptible to nepheloid layers should consider the unique challenges associated with their environment. Whether due to sediment or bacterial accumulation within conductivity cells, deep instruments at KEO experienced conductivity drift which propagated through to the calculation of salinity. To mitigate cumulative contamination from the nepheloid layer or biomass, it is recommended that mooring records overlap with newer deployments. Other recommendations include testing pumped instruments, using a shallower deployment depth to avoid the nepheloid layer, and deploying collocated nephelometers or current meters to verify sediment density and the conditions that lead to partial self-corrections ("flushing" or "clearing" events). Establishing long-term climatologies of *T*/*S* measurements will provide context for the data presented here. Lagrangian measurement platforms such as deep Argo can provide additional verification, complementing Eulerian mooring data.

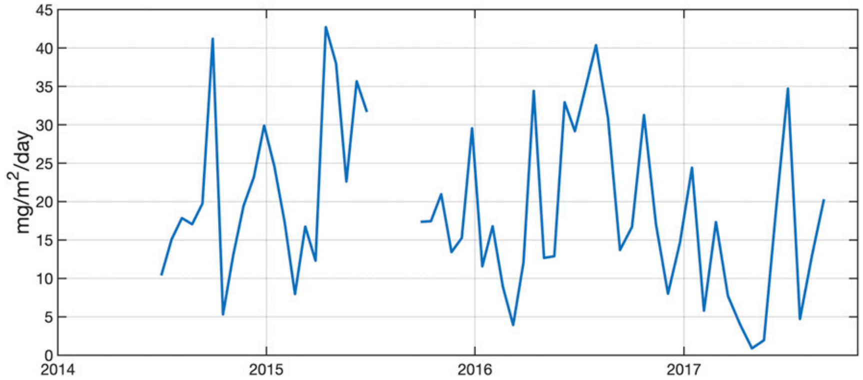

FIG. 13. High lithogenic material fluxes from the JAMSTEC-operated KEO sediment trap may be evidence of a sediment-laden layer.

Efforts guided by these recommendations are already under way. In 2018, additional deep instruments were added to the KEO observational suite: A nonpumped SBE37 measuring $T/C/P$ was placed at ~90 m aof, and a pumped SBE37 (which failed to report usable salinity data) was deployed alongside the standard nonpumped SBE37 at ~56 m aof, for a total of three deep instruments. The two functional instruments, both unpumped, have been included herein, and another pumped instrument is being tested in the 2019–20 deployment. The 90-m instrument was deployed as a first attempt to escape the bottom nepheloid layer, but it remained susceptible to salinity drift. McCave (1986) notes that high turbidity exists in the lowest 1 km of ocean and that nepheloid layers can extend beyond the layer of turbulent mixing, further suggesting that the instrument at 90 m aof remained entrenched in the nepheloid layer. Interestingly, McCave (1986) also notes that nepheloid layers weaken with height, yet surprisingly, salinity drifted more strongly at 90 m aof than at 56 m aof in 2018–19. Less fouling is anticipated with the pumped instrument, as the antifoulant should remain concentrated inside the pumped chamber. Reduced susceptibility to sediment accumulation is also possible, due to the inverted-U shape of the chamber and the active pump. Conversely, this shape could reduce the likelihood of clearing upon ascent for any sediment that manages to infiltrate the chamber. It is hoped that future analysis and continued deployments will guide best practices and provide more insights on measurements within the deep ocean environment.

Acknowledgments. This study benefited from discussions with SeaBird Scientific. The NOAA KEO surface mooring is funded by the U.S. Department of Commerce, NOAA OAR, Global Ocean Monitoring and Observing Program, under NOAA CPO Fund Reference 100007298. Funds supporting the KEO time series sediment trap experiment have come from multiple sources over the years (JAMSTEC Reference a100110/402002; MEXT KAKENHI: JP15H05822 and JP18H04144). This publication is partially funded by the Cooperative Institute for Climate, Ocean, and Ecosystem Studies (CICOES), formerly the Joint Institute for the Study of the Atmosphere and Ocean (JISAO), under NOAA Cooperative Agreement NA15OAR4320063, Contribution 2019-1021. This is PMEL Contribution 5001.

Data availability statement. KESS CPIES data are available at the National Centers for Environmental Information: NODC Accession 0073269. KESS CTD data can be found at the CLIVAR and Carbon Hydrographic Office, expocodes 325020040424, 33RR200050167, and 318M20060601. The altimeter products were produced by SSALTO/DUACS and are distributed by Aviso+, with support from CNES (https://www.aviso.altimetry.fr). Access to all KEO surface mooring data is provided in the text. Data from the KEO ascent are truncated online and therefore are provided in a table in the online supplemental material.

REFERENCES

Aller, J. Y., 1997: Benthic community response to temporal and spatial gradients in physical disturbance within a deep-sea western boundary region. *Deep-Sea Res. I*, **44**, 39–69, https://doi.org/10.1016/S0967-0637(96)00092-1.

Ando, K., T. Matsumoto, T. Nagahama, I. Ueki, Y. Takatsuki, and Y. Kuroda, 2005: Drift characteristics of a mooring conductivity–temperature–depth sensor and correction of salinity data. *J. Atmos. Oceanic Technol.*, **22**, 282–291, https://doi.org/10.1175/JTECH1704.1.

Bishop, S. P., D. R. Watts, and K. A. Donohue, 2013: Divergent eddy heat fluxes in the Kuroshio Extension at 144°–148°E. Part I: Mean structure. *J. Phys. Oceanogr.*, **43**, 1533–1550, https://doi.org/10.1175/JPO-D-12-0221.1.

Bretherton, C. S., M. Widmann, V. P. Dymnikov, J. M. Wallace, and I. Bladé, 1999: The effective number of spatial degrees of freedom of a time-varying field. *J. Climate*, **12**, 1990–2009, https://doi.org/10.1175/1520-0442(1999)012<1990:TENOSD>2.0.CO;2.

Bretherton, F. P., R. E. Davis, and C. B. Fandry, 1976: A technique for objective analysis and design of oceanographic experiments applied to MODE-73. *Deep-Sea Res. Oceanogr. Abstr.*, **23**, 559–582, https://doi.org/10.1016/0011-7471(76)90001-2.

Cronin, M. F., T. Tozuka, A. Biastoch, J. V. Durgadoo, and L. M. Beal, 2013: Prevalence of strong bottom currents in the greater Agulhas system. *Geophys. Res. Lett.*, **40**, 1772–1776, https://doi.org/10.1002/grl.50400.

Donohue, K., and Coauthors, 2008: Program studies the Kuroshio Extension. *Eos, Trans. Amer. Geophys. Union*, **89**, 161–162, https://doi.org/10.1029/2008EO170002.

Fischer, A. S., J. Hall, D. E. Harrison, D. Stammer, and J. Benveniste, 2010: Ocean information for society: Sustaining the benefits, realizing the potential. *Proc. OceanObs'09: Sustained Ocean Observations and Information for Society*, Venice, Italy, ESA, WPP-306, https://doi.org/10.5270/OceanObs09.Summary.

Fofonoff, N., and R. Millard, 1983: Algorithms for computation of fundamental properties of seawater. UNESCO Tech. Paper in Marine Science 44, 58 pp., http://unesdoc.unesco.org/images/0005/000598/059832eb.pdf.

Francois, R., S. Honjo, R. Krishfield, and S. Manganini, 2002: Factors controlling the flux of organic carbon to the bathypelagic zone of the ocean. *Global Biogeochem. Cycles*, **16**, 1087, https://doi.org/10.1029/2001GB001722.

Freitag, H. P., M. E. McCarty, C. Nosse, R. Lukas, M. J. McPhaden, and M. F. Cronin, 1999: COARE Seacat data: Calibrations and quality control procedures. NOAA Tech. Memo., ERL PMEL-115, 89 pp., https://www.pmel.noaa.gov/pubs/PDF/frei2034/frei2034.pdf.

Gage, J. D., 1996: Why are there so many species in deep-sea sediments? *J. Exp. Mar. Biol. Ecol.*, **200**, 257–286, https://doi.org/10.1016/S0022-0981(96)02638-X.

Gardner, W. D., B. E. Tucholke, M. J. Richardson, and P. E. Biscaye, 2017: Benthic storms, nepheloid layers, and linkage with upper ocean dynamics in the western North Atlantic. *Mar. Geol.*, **385**, 304–327, https://doi.org/10.1016/j.margeo.2016.12.012.

——, M. J. Richardson, A. V. Mishonov, and P. E. Biscaye, 2018a: Global comparison of benthic nepheloid layers based on 52 years of nephelometer and transmissometer measurements. *Prog. Oceanogr.*, **168**, 100–111, https://doi.org/10.1016/j.pocean.2018.09.008.

——, ——, and ——, 2018b: Global assessment of benthic nepheloid layers and linkage with upper ocean dynamics. *Earth Planet. Sci. Lett.*, **482**, 126–134, https://doi.org/10.1016/j.epsl.2017.11.008.

Greene, A. D., D. R. Watts, G. G. Sutyrin, and H. Sasaki, 2012: Evidence of vertical coupling between the Kuroshio Extension and topographically controlled deep eddies. *J. Mar. Res.*, **70**, 719–747, https://doi.org/10.1357/002224012806290723.

Gross, T. F., and A. J. Williams III, 1991: Characterization of deep-sea storms. *Mar. Geol.*, **99**, 281–301, https://doi.org/10.1016/0025-3227(91)90045-6.

Heuzé, C., K. J. Heywood, D. P. Stevens, and J. K. Ridley, 2015: Changes in global ocean bottom properties and volume transports in CMIP5 models under climate change scenarios. *J. Climate*, **28**, 2917–2944, https://doi.org/10.1175/JCLI-D-14-00381.1.

Hollister, C. D., and I. N. McCave, 1984: Sedimentation under deep-sea storms. *Nature*, **309**, 220–225, https://doi.org/10.1038/309220a0.

Honda, M. C., K. Imai, Y. Nojiri, F. Hoshi, T. Sugawara, and M. Kusakabe, 2002: The biological pump in the northwestern North Pacific based on fluxes and major components of particulate matter obtained by sediment trap experiments (1997-2000). *Deep-Sea Res. II*, **49**, 5595–5625, https://doi.org/10.1016/S0967-0645(02)00201-1.

——, Y. Sasai, E. Siswanto, A. Kuwano-Yoshida, H. Aiki, and M. F. Cronin, 2018: Impact of cyclonic eddies and typhoons on biogeochemistry in the oligotrophic ocean based on biogeochemical/physical/meteorological time series at station KEO. *Prog. Earth Planet. Sci.*, **5**, 42, https://doi.org/10.1186/s40645-018-0196-3.

Johnson, G. C., J. M. Lyman, and S. G. Purkey, 2015: Informing Deep Argo array design using Argo and full-depth hydrographic section data. *J. Atmos. Oceanic Technol.*, **32**, 2187–2198, https://doi.org/10.1175/JTECH-D-15-0139.1.

——, S. G. Purkey, N. V. Zilbermann, and D. Roemmich, 2019: Deep Argo quantifies bottom water warming rates in the southwest Pacific basin. *Geophys. Res. Lett.*, **46**, 2662–2669, https://doi.org/10.1029/2018GL081685.

Kämpf, J., 2005: Cyclogenesis in the deep ocean beneath western boundary currents: A process-oriented numerical study. *J. Geophys. Res.*, **110**, C03001, https://doi.org/10.1029/2003JC002206.

Lamborg, C. H., and Coauthors, 2008: The flux of bio- and lithogenic material associated with sinking particles in the mesopelagic ''twilight zone'' of the northwest and north central Pacific Ocean. *Deep-Sea Res. II*, **55**, 1540–1563, https://doi.org/10.1016/j.dsr2.2008.04.011.

Levin, L. A., and Coauthors, 2019: Global observing needs in the deep ocean. *Front. Mar. Sci.*, **6**, 241, https://doi.org/10.3389/fmars.2019.00241.

Masuda, S., and Coauthors, 2010: Simulated rapid warming of abyssal North Pacific waters. *Science*, **329**, 319–322, https://doi.org/10.1126/science.1188703.

McCave, I. N., 1986: Local and global aspects of the bottom nepheloid layers in the World Ocean. *Neth. J. Sea Res.*, **20**, 167–181, https://doi.org/10.1016/0077-7579(86)90040-2.

McLennan, S. M., 2001: Relationships between the trace element composition of sedimentary rocks and upper continental crust. *Geochem. Geophys. Geosyst.*, **2**, 1021, https://doi.org/10.1029/2000GC000109.

Na, H., D. R. Watts, J.-H. Park, C. Jeon, H. J. Lee, M. Nonaka, and A. D. Greene, 2016: Bottom pressure variability in the Kuroshio Extension driven by the atmosphere and ocean instabilities. *J. Geophys. Res. Oceans*, **121**, 6507–6519, https://doi.org/10.1002/2016JC012097.

Oka, E., 2005: Long-term sensor drift found in recovered Argo profiling floats. *J. Oceanogr.*, **61**, 775–781, https://doi.org/10.1007/s10872-005-0083-6.

——, and K. Ando, 2004: Stability of temperature and conductivity sensors of Argo profiling floats. *J. Oceanogr.*, **60**, 253–258, https://doi.org/10.1023/B:JOCE.0000038331.10108.79.

Otosaka, S., O. Togawa, M. Baba, E. Karasev, Y. N. Volkov, N. Omata, and S. Noriki, 2004: Lithogenic flux in the Japan Sea measured with sediment trap. *Mar. Chem.*, **91**, 143–163, https://doi.org/10.1016/j.marchem.2004.06.006.

Park, J. H., D. R. Watts, K. A. Donohue, and S. R. Jayne, 2008: A comparison of in situ bottom pressure array measurements with GRACE estimates in the Kuroshio Extension. *Geophys. Res. Lett.*, **35**, L17601, https://doi.org/10.1029/2008GL034778.

——, K. A. Donohue, D. R. Watts, and L. Rainville, 2010: Distribution of deep near-inertial waves observed in the Kuroshio Extension. *J. Oceanogr.*, **66**, 709–717, https://doi.org/10.1007/s10872-010-0058-0.

Purkey, S. G., and G. C. Johnson, 2010: Warming of global abyssal and deep Southern Ocean waters between the 1990s and 2000s: Contributions to global heat and sea level rise budgets. *J. Climate*, **23**, 6336–6351, https://doi.org/10.1175/2010JCLI3682.1.

——, ——, L. D. Talley, B. M. Sloyan, S. E. Wijffels, W. Smethie, S. Mecking, and K. Katsumata, 2019: Unabated bottom water warming and freshening in the South Pacific Ocean. *J. Geophys. Res. Oceans*, **124**, 1778–1794, https://doi.org/10.1029/2018JC014775.

Qiu, B., and S. Chen, 2006: Decadal variability in the formation of the North Pacific subtropical mode water: Oceanic versus atmospheric control. *J. Phys. Oceanogr.*, **36**, 1365–1380, https://doi.org/10.1175/JPO2918.1.

——, and ——, 2010: Eddy-mean flow interaction in the decadally modulating Kuroshio Extension system. *Deep-Sea Res. II*, **57**, 1098–1110, https://doi.org/10.1016/j.dsr2.2008.11.036.

——, ——, N. Schneider, and B. Taguchi, 2014: A coupled decadal prediction of the dynamic state of the Kuroshio Extension system. *J. Climate*, **27**, 1751–1764, https://doi.org/10.1175/JCLI-D-13-00318.1.

——, ——, L. Wu, and S. Kida, 2015: Wind- versus eddy-forced regional sea level trends and variability in the North Pacific Ocean. *J. Climate*, **28**, 1561–1577, https://doi.org/10.1175/JCLI-D-14-00479.1.

Quirchmayr, R., 2015: On the existence of benthic storms. *J. Nonlinear Math. Phys.*, **22**, 540–544, https://doi.org/10.1080/14029251.2015.1113053.

Rainville, L., S. R. Jayne, and M. F. Cronin, 2014: Variations of the North Pacific subtropical mode water from direct observations. *J. Climate*, **27**, 2842–2860, https://doi.org/10.1175/JCLI-D-13-00227.1.

Rhein, M., and Coauthors, 2013: Observations: Ocean. *Climate Change 2013: The Physical Science Basis*, T. F. Stocker et al., Eds., Cambridge University Press, 255–315, https://doi.org/10.1017/CBO9781107415324.010.

Richardson, M. J., G. L. Weatherly, and W. D. Gardner, 1993: Benthic storms in the Argentine basin. *Deep-Sea Res. II*, **40**, 975–987, https://doi.org/10.1016/0967-0645(93)90044-N.

Roemmich, D., and Coauthors, 2019: Deep SOLO: A full depth profiling float for the Argo program. *J. Atmos. Oceanic Technol.*, **36**, 1967–1981, https://doi.org/10.1175/JTECH-D-19-0066.1.

Schubert, R., A. Biastoch, M. F. Cronin, and R. J. Greatbatch, 2018: Instability-driven benthic storms below the separated Gulf Stream and the North Atlantic Current in a high-resolution ocean model. *J. Phys. Oceanogr.*, **48**, 2283–2303, https://doi.org/10.1175/JPO-D-17-0261.1.

Smith, W. H. F., and D. T. Sandwell, 1997: Global seafloor topography from satellite altimetry and ship depth soundings. *Science*, **277**, 1956–1962, https://doi.org/10.1126/science.277.5334.1956.

Thadathil, P., C. C. Bajish, S. Behera, and V. V. Gopalakrishna, 2012: Drift in salinity data from Argo profiling floats in the Sea of Japan. *J. Atmos. Oceanic Technol.*, **29**, 129–138, https://doi.org/10.1175/JTECH-D-11-00018.1.

Tracey, K. L., D. R. Watts, K. A. Donohue, and H. Ichikawa, 2012: Propagation of Kuroshio extension meanders between 143° and 149° E. *J. Phys. Oceanogr.*, **42**, 581–601, https://doi.org/10.1175/JPO-D-11-0138.1.

——, K. A. Donohue, and D. R. Watts, 2017: Bottom temperatures in Drake Passage. *J. Phys. Oceanogr.*, **47**, 101–122, https://doi.org/10.1175/JPO-D-16-0124.1.

Ueki, I., and T. Nagahama, 2005: Evaluation of property change of pressure sensor installed on TRITON buoys. JAMSTEC Rep. of Research and Development 1, 51–55, http://www.godac.jamstec.go.jp/catalog/data/doc_catalog/media/JAM_RandD01_06.pdf.

Venkatesan, R., K. Ramesh, M. Arul Muthiah, K. Thirumurugan, and M. Aravindakshan Atmanand, 2019: Analysis of drift characteristic in conductivity and temperature sensors used in moored buoy system. *Ocean Eng.*, **171**, 151–156, https://doi.org/10.1016/j.oceaneng.2018.10.033.

Waterman, S., N. G. Hogg, and S. R. Jayne, 2011: Eddy–mean flow interaction in the Kuroshio Extension region. *J. Phys. Oceanogr.*, **41**, 1182–1208, https://doi.org/10.1175/2010JPO4564.1.

WCRP, 1988: World Ocean Circulation Experiment implementation plan: Detailed requirements. WMO Rep. WMO/TD 242, Vol. I, 63 pp., https://www.nodc.noaa.gov/woce/wdiu/wocedocs/impplan/vol1.pdf.

Yang, Y., X. San Liang, B. Qiu, and S. Chen, 2017: On the decadal variability of the eddy kinetic energy in the Kuroshio Extension. *J. Phys. Oceanogr.*, **47**, 1169–1187, https://doi.org/10.1175/JPO-D-16-0201.1.

Zhang, M., Z. Wu, and F. Qiao, 2018: Deep Atlantic Ocean warming facilitated by the deep western boundary current and equatorial Kelvin waves. *J. Climate*, **31**, 8541–8555, https://doi.org/10.1175/JCLI-D-18-0255.1.